

Geophysical Research Letters[®]

RESEARCH LETTER

10.1029/2022GL098161

Special Section:

ExoMars Trace Gas Orbiter -
One Martian Year of Science

Key Points:

- A full Martian year of water and D/H ratio data are reported
- Dramatic variations are observed in the vertical distributions of water and D/H during the dusty seasons
- The D/H ratio measured above the seasonal northern polar cap is consistent with that above the southern polar cap

Correspondence to:

G. L. Villanueva,
geronimo.villanueva@nasa.gov

Citation:

Villanueva, G. L., Liuzzi, G., Aoki, S., Stone, S. W., Brines, A., Thomas, I. R., et al. (2022). The deuterium isotopic ratio of water released from the Martian caps as measured with TGO/NOMAD. *Geophysical Research Letters*, 49, e2022GL098161. <https://doi.org/10.1029/2022GL098161>

Received 1 FEB 2022

Accepted 30 MAY 2022

Author Contributions:

Conceptualization: Geronimo L. Villanueva, Giuliano Liuzzi
Data curation: Geronimo L. Villanueva, Giuliano Liuzzi, Ian R. Thomas, Justin Erwin, Bojan Ristic, Michael D. Smith, Ann Carine Vandaele
Formal analysis: Geronimo L. Villanueva, Giuliano Liuzzi
Funding acquisition: Geronimo L. Villanueva, Michael D. Smith, Michael J. Mumma, Giancarlo Bellucci, Jose Juan Lopez-Moreno, Ann Carine Vandaele
Investigation: Geronimo L. Villanueva, Giuliano Liuzzi, Shohei Aoki, Ian R. Thomas, Miguel Angel Lopez-Valverde, Frank Daerden, Michael J. Mumma, Lori Neary, Manish Patel, Ann Carine Vandaele

© 2022 American Geophysical Union.
All Rights Reserved. This article has
been contributed to by U.S. Government
employees and their work is in the public
domain in the USA.

The Deuterium Isotopic Ratio of Water Released From the Martian Caps as Measured With TGO/NOMAD

Geronimo L. Villanueva¹ , Giuliano Liuzzi^{1,2} , Shohei Aoki³ , Shane W. Stone^{1,4} ,
Adrian Brines⁵ , Ian R. Thomas⁶ , Miguel Angel Lopez-Valverde⁵ , Loic Trompet⁶ ,
Justin Erwin⁶ , Frank Daerden⁶ , Bojan Ristic⁶ , Michael D. Smith¹ ,
Michael J. Mumma¹ , Sara Faggi^{1,2} , Vincent Kofman^{1,2} , Séverine Robert^{6,7} ,
Lori Neary⁶ , Manish Patel⁸ , Giancarlo Bellucci⁹ , Jose Juan Lopez-Moreno⁵ , and
Ann Carine Vandaele⁶ 

¹Planetary Systems Laboratory, NASA Goddard Space Flight Center, Greenbelt, MD, USA, ²Physics Department, American University, Washington, DC, USA, ³Graduate School of Frontier Sciences, University of Tokyo, Japan, ⁴NPP/USRA, Goddard Space Flight Center, Greenbelt, MD, USA, ⁵Instituto de Astrofísica de Andalucía, CSIC, Spain, ⁶Planetary Aeronomy Division, Royal Belgian Institute for Space Aeronomy, Belgium, ⁷Institute of Condensed Matter and Nanosciences, Université catholique de Louvain, Belgium, ⁸School of Physical Sciences, The Open University, UK, ⁹Istituto di Astrofisica e Planetologia Spaziali, INAF, Italy

Abstract We report vertical profiles of water and D/H for one Martian year as measured with the TGO/NOMAD instrument. The observations were performed via solar occultation, providing water profiles up to ~100 km and D/H up to ~60 km, with a vertical resolution of 1–2 km. The measurements reveal dramatic variability of water and D/H over short timescales and with altitude and location on the planet. We investigated the release of seasonal water from the polar caps during southern and northern summer, by mapping water and its D/H near the polar regions. Above the hygropause, the D/H drops substantially below 2 VSMOW, and both seasonal polar caps show a consistent and enriched D/H of 5–7 VSMOW within the hygrosphere.

Plain Language Summary In our observations of water and its deuterium isotopic ratio (D/H) across a whole Martian year, we observe dramatic variations in the vertical distributions, in particular during dusty storms. The D/H ratio measured above the seasonal northern polar cap is consistent with that above the southern polar cap.

1. Introduction

The evolution and history of water on Mars plays a key role in the assessment of the habitability of the planet across time. There is abundant geomorphological evidence suggesting that Mars had a wetter past (Bibring et al., 2006; Carr & Head, 2003), yet the duration and extent of this more humid past remains a topic of substantial debate. For instance, the large deltas, basins, and valleys on Mars are suggestive of large bodies of water that were stable over relatively long periods of time. Some estimates suggest past volumes of water in excess of a 500 m deep Global Equivalent Layer (GEL; Carr & Head, 2003), which is many times larger than the current estimates of labile water on Mars (~30 m, Lasue et al., 2013).

The large enrichments of D/H measured in atmospheric water suggest that a large fraction, beyond 80%, of this water was lost over time (Jakosky, 2021; Villanueva et al., 2015), and Ar and O isotopic ratios measured with MAVEN (Jakosky et al., 2017) and TGO (Alday, Wilson, et al., 2021) indicate that Mars has lost a large fraction of its atmosphere. Because Mars is less massive than Earth, the neutral escape of volatiles is easier on Mars, considering the similar equilibrium temperatures of the two planets, although Mars is obviously colder. Recent results indicate that most of this escape occurred via neutral and nonionized processes (Brain et al., 2015), in which temperature and its variability across geological times were key factors defining the state of the Martian atmosphere. Recent results from dust storms suggest that dust storms can greatly heat the atmosphere, leading to the upward transport and more readily escape of water (Aoki et al., 2019; Belyaev et al., 2021; Chaffin et al., 2021; Fedorova et al., 2020; Heavens et al., 2018; Holmes et al., 2021; Neary et al., 2020; Stone et al., 2020).

As we attempt to trace back the history of water on Mars, it is unknown how much water remains locked in nonlabile/subsurface reservoirs. In addition, the currently known reservoirs may exchange and lose water over time at

Methodology: Geronimo L. Villanueva, Giuliano Liuzzi, Shohei Aoki, Adrian Brines, Ian R. Thomas, Miguel Angel Lopez-Valverde, Loic Trompet, Justin Erwin, Frank Daerden, Michael D. Smith, Sara Faggi, Vincent Kofman, Séverine Robert, Ann Carine Vandaele

Project Administration: Geronimo L. Villanueva, Michael D. Smith, Michael J. Mumma, Manish Patel, Giancarlo Bellucci, Jose Juan Lopez-Moreno, Ann Carine Vandaele

Resources: Geronimo L. Villanueva, Giuliano Liuzzi, Ian R. Thomas, Ann Carine Vandaele

Software: Geronimo L. Villanueva, Giuliano Liuzzi, Adrian Brines, Ian R. Thomas, Miguel Angel Lopez-Valverde, Sara Faggi, Vincent Kofman

Supervision: Geronimo L. Villanueva

Validation: Geronimo L. Villanueva, Giuliano Liuzzi, Shohei Aoki, Adrian Brines, Ian R. Thomas, Miguel Angel Lopez-Valverde, Loic Trompet, Justin Erwin, Frank Daerden, Ann Carine Vandaele

Visualization: Geronimo L. Villanueva, Giuliano Liuzzi, Adrian Brines, Ian R. Thomas, Miguel Angel Lopez-Valverde

Writing – original draft: Geronimo L. Villanueva

Writing – review & editing: Geronimo L. Villanueva, Giuliano Liuzzi, Shohei Aoki, Adrian Brines, Ian R. Thomas, Miguel Angel Lopez-Valverde, Frank Daerden, Michael J. Mumma, Sara Faggi, Vincent Kofman, Séverine Robert, Lori Neary, Manish Patel, Ann Carine Vandaele

different rates, and those processes responsible are still poorly understood (Scheller et al., 2021). The polar caps are the most studied reservoirs of water on Mars, corresponding to 11 m GEL for the southern polar cap (Plaut et al., 2007), and 10 m GEL for the northern polar cap (Zuber et al., 1998). The polar ice is composed of a basal unit that has been estimated to be a billion years old (Byrne & Murray, 2002; Fishbaugh & Head, 2005), on top of which lie the stratified deposits at the north pole that are likely to be younger ice, in particular, considering the frequent and large inclination variations that have occurred over time and their associated global climate change. An important question is then whether all current labile reservoirs have evolved in the same way and undergone extensive exchange. In principle, the isotopic signatures among these reservoirs should then be identical, and as such the investigation of distinct isotopic signatures across reservoirs provides a way to track the level of exchange between reservoirs.

Considering the ratio of water stored in the polar caps with what circulates today in the atmosphere (1 million times smaller), for all reservoirs to share the same D/H, the hydrological cycle in the past would have to be sufficiently stronger and sustained over long period of times. Only a small layer of water (μm GEL levels) is released seasonally from the caps every year during the local summer. The water subliming from the south polar region in spring and summer was deposited in fall and winter and thus only reveals the composition of the seasonal water cycling back and forth between the poles (Houben et al., 1997; Richardson & Wilson, 2002). In the north, this aspect is complicated by the uncertainty about the partitioning between old ice and seasonally recycled ice in the sublimation flux. Whether this seasonal layer describes the underlying meters of water ice in the caps is a topic of extensive debate (Jakosky, 2021). Yet, if the caps were formed by climatological and seasonal patterns similar to those driving the circulation today, then this seasonally released water should have the same isotopic signature across both hemispheres and should describe the underlying ice caps. If, on the other hand, their isotopic signatures are distinct, it would indicate that reservoirs evolve quite differently over time on Mars, and a unifying evolution and escape path for them does not apply.

Mapping of the water D/H during northern summer revealed an enriched value of D/H around 6–7 VSMOW for the water being released seasonally from the northern polar cap (Krasnopolsky, 2015; Villanueva et al., 2015). The observations were done employing ground-based observatories and probe the whole atmospheric column at specific dates over a full planetary hemisphere. Similarly enriched D/H values were observed during southern summer via solar-occultation (SO) measurements with TGO/Nadir and Occultation for MArS Discovery (NOMAD; Villanueva et al., 2021) and TGO/ACS (Alday, Trokhimovskiy, et al., 2021), yet the measurement technique is quite different to the previously reported ground-based observations, so direct comparisons between the seasonal release from polar caps may not be straightforward. Specifically, TGO probes each altitude separately and does not provide information on water below ~ 10 km (due to limb/tangential aerosols extinction), with global and seasonal mapping being achieved by combining data over a large time span. The ground-based data, on the other hand, provide snapshots in time of the integrated water column across all altitudes for points across the observable disk.

We have now analyzed data over the entirety a Martian year as measured with TGO/NOMAD, which probed the release of water from the two polar caps using the instrument's SO mode, enabling an investigation of the vertical structure of the isotopic signatures across the planet and above the two main water reservoirs. This analysis makes use of improved instrument calibration procedures and of the latest spectroscopic data for water and carbon dioxide in a CO_2 -rich atmosphere. We present details about the new calibration methods in Section 2 and in Appendix A. A discussion on the observed values for water and D/H across the planet is presented in Section 3, while a summary and conclusions, including analysis regarding the exchange between water reservoirs and implications for the history of water on Mars, are presented in Section 4.

2. Data Sets and Methods

The measurements presented here have been collected by the NOMAD (Neefs et al., 2015; Vandaele et al., 2019) instrument suite onboard TGO, which probes the atmospheric composition using high-resolution infrared spectroscopy. The data were collected employing the SO channel/mode of the instrument, in which the atmosphere is probed sequentially in altitude by pointing to the Sun and measuring the absorption due to molecules and aerosols across the tangential line of sight. The SO channel operates at wavelengths between 2.2 and 4.3 μm , in which HDO is primarily probed via its ν_1 band at 3.7 μm (orders 119–121 of the instrument), and H_2O is probed via

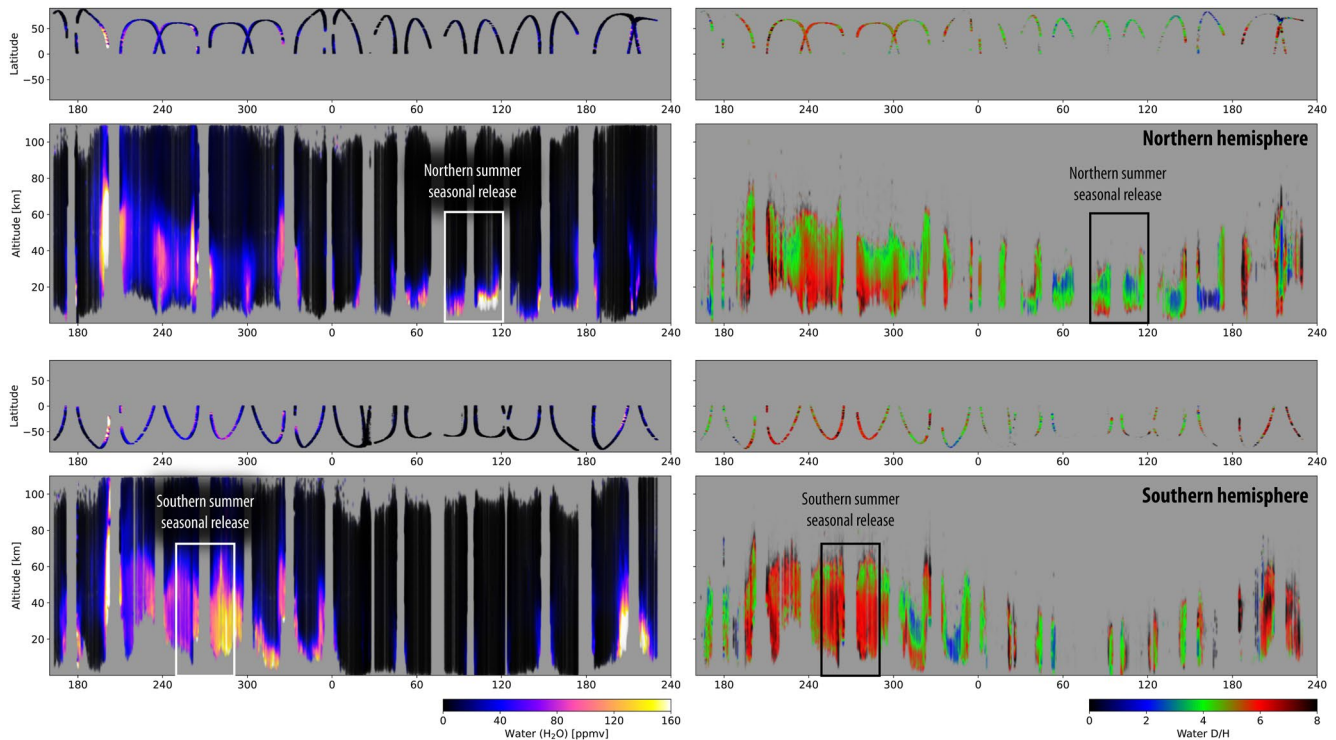


Figure 1. Seasonal evolution of water and its D/H across a full Martian year, starting on MY34 and ending on $L_S = 240$ MY35. Only H_2O values with uncertainties lower than 15 ppmv and D/H values with sigma lower than 1 VSMOW are shown. The global dust storm and the large regional dust storm that took place during $L_S = 190$ to $L_S = 360$ of MY34 greatly modified the atmosphere and brought water to very high altitudes. In all cases, the D/H drops notably beyond the hygropause to 1–2 VSMOW, and the profiles show an enriched value of 5–7 VSMOW within the hygrosphere. The hygrosphere can be challenging to properly sample, since in many cases it extends only to altitudes less than 20 km and is close to the detection limit via occultation. The latitude subpanels indicate the sampled latitudes during that season and the colors indicate average value for that season.

different bands in the 2.7–3.3 μm region (orders 133–170). The NOMAD instrument is an echelle high-resolution grating spectrometer, in which an Acousto-Optical-Tunable-Filter (AOTF) operates as an order-sorting device. Typically, 5–6 orders are sampled per altitude, targeting the ν_1 of HDO, several bands of H_2O , CO_2 , CO, and trace gases. The instrument's sensitivity to the ν_1 band of HDO enables meaningful measurements of the HDO abundance at altitudes less than 60–70 km, and measurements of the H_2O abundance can be obtained up to 110 km altitude by probing multiple absorption bands including the ν_3 fundamental. The vertical resolution is defined by the integration times, orbital speed, and inclination, with typical sampling of 1–2 km. Seasonal maps as those presented in Figure 1 are created by aggregating data across several occultations and range of solar longitude (L_S), which are taken with a cadence of 11–14 NOMAD occultations per sol (see details in Villanueva et al., 2021)— H_2O : 126, 127 (2%), 130, 133, 134, 135, 136 (59%), 143, 145, 153, 154 (5%), 167, 168, 169, 170, 171 (36%); HDO: 116, 118, 119 (22%), 121 (63%), 124, 126, 127 (15%).

Retrievals are performed on level 1 calibrated data as processed by the NOMAD team (Liuzzi et al., 2019; Thomas et al., 2021). The spectra are computed by normalizing the data at each occultation to a reference spectrum of the Sun derived from data at high altitudes (>200 km) during the occultation. A challenge in the interpretation of NOMAD data is that it records overlapping signatures from nearby orders introduced by the AOTF plus grating configuration of the instrument. As the instrument is tuned to a specific order, the filter permits signal from that and nearby orders to pass through to the detector, so the observed spectrum is a combination of signal from several orders. Interpretation of molecular signatures in such a spectrum is then susceptible to the considered AOTF response functions, grating parameters, and the Instrument Line Shape (ILS) kernel (Liuzzi et al., 2019; Villanueva et al., 2021). For that purpose, detailed work was undertaken by the NOMAD team to characterize the properties of the instrument with high accuracy by employing several calibration data campaigns and Mars observations. The AOTF response function is primarily described as an asymmetric sinc function, the grating follows a parameterized grating equation, and the ILS is represented by a double Gaussian kernel. Several

retrievals and analytical methods were performed on the data to check for consistency among these calibration solutions. Detailed information about the calibration “recipe” and characterization of the instrument response function is presented in Appendix A.

Interpretation and extraction of molecular abundances from the calibrated data is done by employing the Planetary Spectrum Generator (<https://psg.gsfc.nasa.gov>, Villanueva et al., 2018), and as reported in Villanueva et al., 2021 (please refer to this paper for more details on the retrieval methods). The model employs a layer-by-layer line-by-line method in a spherical and refractive geometry. We employ the latest linelists for H₂O, HDO, and CO₂ as compiled in the HITRAN-2020 database (Gordon et al., 2022), which are complemented to include the latest H₂O and HDO broadening coefficients for a CO₂ atmosphere (Devi et al., 2017; Régalia et al., 2019). Each occultation spectrum is treated as an independent measurement, and retrievals are performed by employing an optimal estimation approach for all molecules having signatures in the order. If the same molecule is sampled among many diffraction orders during that occultation, the results are combined and weighted based on their individual uncertainties. The D/H ratio is derived from the weighted averages of H₂O and HDO. For the a priori temperature and density profiles considered for the retrievals, we extracted climatological data from the GEM Martian Climate model (Neary & Daerden, 2018), which has been specifically parameterized for MY34 (Daerden et al., 2022; Neary et al., 2020).

In order to minimize systematic effects related to the a priori climatology in our retrievals, only retrievals sampling H₂O and HDO simultaneously (within 2 s) are considered in this report. Effectively, both retrievals sample the slant path across the same locations, altitudes, and time. The assumed temperature will nevertheless each order retrieval differently, depending on the excitation energy of the sampled lines. For instance, the HDO retrievals (orders 116–126) and the H₂O retrievals employing the ν_3 band (orders 167–171) primarily target low-J lines, while the H₂O retrievals of the $2\nu_2$ band (orders 133–136) sample higher J lines. We have previously explored the impact of this in detail (Villanueva et al., 2021), and generally we obtain consistent results between water retrievals between different orders (Figure S6 in Villanueva et al., 2021), implying a relatively good compensation for the temperature issue. Furthermore, the possibility to access different absorption bands of water also helps to mitigate opacity issues. For instance, strong fundamental bands of H₂O (e.g., ν_3) probe water up to 110 km, but become more saturated beyond 50 km, while the weaker $2\nu_2$ band probes deeper into the atmosphere without saturation and have comparable opacity to the HDO lines. There is no active rejection criteria to produce these figures. All the spectra at all altitudes up to 110 km are processed, apart from the spectra whose I/F is lower than 3% (low altitudes). In the maps, all the data are weighed based on the retrieval uncertainty. Detailed reports of the error-analysis, order combination, error propagation, and accuracy of the retrievals are presented in Villanueva et al. (2021). Considering the peak uncertainties presented in Figures S6 and S7 of Villanueva et al. (2021) and the challenges discussed above, we assume a conservative error-bar of 1 VSMOW for the D/H, and 10 ppmv for the H₂O reported in Figure 1.

3. The Seasonal and Spatial Variability of the D/H

During Martian year 34, the planet was engulfed in a global dust storm (GDS) that greatly perturbed the temperature and vertical structure of the Martian atmosphere. The GDS started just after the southern spring equinox ($L_s > 180^\circ$), and lasted primarily until $L_s = 240^\circ$ (Montabone et al., 2020), yet its effects on the atmosphere may have lasted longer. In addition, the lingering effects of the GDS were joined by a large regional dust storm that started during late southern summer ($L_s \sim 320^\circ$). These two major events greatly affected the climate of Mars, primarily leading to a strong increase in atmospheric temperature, a substantial rise in altitude of the hygropause, and subsequent transport of water to unexpectedly high altitudes (Aoki et al., 2019; Belyaev et al., 2021; Chaffin et al., 2021; Heavens et al., 2018; Holmes et al., 2021; Neary et al., 2020; Stone et al., 2020).

After the northern spring equinox, the atmosphere returned to a state consistent with regular seasonal trends. The dramatic impact of these storms on the vertical distribution of water and the D/H can be observed in Figure 1, in which water is shown to reach high altitudes during the main part of the GDS ($L_s = 200^\circ$ – 220°) and during periapsis at southern summer ($L_s 270^\circ$ – 300°). Modeling of the D/H cycle with a General Circulation Model was recently performed (Daerden et al., 2022) to demonstrate the impact of the GDS compared to a normal situation. These simulations, in direct comparison with the NOMAD D/H observations, showed also how the effects of the GDS were mostly over by $L_s \sim 230^\circ$ (Daerden et al., 2022, their Figure 18). Interestingly, during the GDS

when the Northern Hemisphere was in the winter season, the climate was substantially warmer there than normal (Daerden et al., 2022; Montabone et al., 2020; Rossi et al., 2021), leading to high-altitude water also in the Northern Hemisphere. Typically, the largest seasonal water columns are observed during summer in the Northern Hemisphere (Crismani et al., 2021), and that may be true in MY35, but the vertical profile of water is highly compact (confined to altitudes below 20 km), even at the peak of northern summer ($L_S \sim 90\text{--}130^\circ$). This was already anticipated from cloud detections in northern summer by the Phoenix mission (Whiteway et al., 2009) and their simulated impact on the vertical distribution of water vapor (Daerden et al., 2010). (Note: GCM simulations shown in Daerden et al. (2022) do not sufficiently confine water vapor so low due to a simplistic cloud description.). In all cases (all seasons and regions of the planet), the D/H declines quickly above the hygropause, from a nominal value above 5 VSMOW to a very low value near <2 VSMOW when HDO is not present (owing to its preferential freeze-out). This is consistent with our initial reports in Villanueva et al. (2021) and GCM modeling (Daerden et al., 2022; Rossi et al., 2021), as well as complementary measurements with the ACS spectrometer suite (Alday, Trokhimovskiy, et al., 2021), which highlights the strong variability of this parameter with altitude. Alday, Trokhimovskiy, et al. (2021) reports a D/H greater than 5–6 VSMOW during southern summer ($L_S \sim 190^\circ\text{--}300^\circ$) in the 10–60 km altitude range, consistent within error-bars (1 VSMOW) with our findings as reported in Figure 1, which show red colors (~ 6 VSMOW) for this season/altitude. In MY35, localized mid-altitude water with an enriched D/H value is observed during northern fall ($L_S 170^\circ\text{--}190^\circ$) in the Northern Hemisphere and in the Southern Hemisphere during mid southern spring ($L_S 200^\circ\text{--}220^\circ$).

Our SO measurements are not sensitive to the lower 5–10 km of the atmosphere, and therefore they mostly provide information on the “upper” half of the hygropause during the Northern Hemisphere seasonal water release ($L_S 0^\circ\text{--}180^\circ$). Establishing the D/H of the total column from occultation measurements can therefore be challenging, since most of the effective column is not measured and the D/H ratio drops substantially with altitude. For the values during the peak of the northern summer release ($L_S \sim 80^\circ\text{--}130^\circ$) and closer to the surface, the D/H varies in the range of 4–7 VSMOW near the hygropause. Our previous ground-based observations of the total water column (Villanueva et al., 2015), at $L_S \sim 80^\circ$ and primarily weighted to the lower part of the hygropause, indicate a typical D/H of ~ 7 VSMOW for the Northern Hemisphere seasonal release. Assuming as reference the other seasons as shown in Figure 2 and complementary isotopic fractionation modeling (Daerden et al., 2022), a value of $\sim 5\text{--}7$ VSMOW close to the hygropause as reported here is consistent with the previous ground-based observations. Importantly, this would mean that the D/H of the water liberated from the seasonal northern polar cap is the same as that of the water liberated from the seasonal southern polar cap, roughly 6–7 VSMOW. Yet, due to the confinement of water relatively close to the surface during northern summer (see Figures 1 and 2), and the challenges associated with SO probing of such narrow vertical region, our results cannot rule out an alternative scenario with a D/H different than that of the southern seasonal cap. Future ground-based mapping during Mars southern summer could also help to address this question, while as we learn more about the pronounced localized and seasonal D/H variability on Mars, it becomes evident that highly parameterized GCM models with realistic fractionation/cloud models are ultimately needed for interpreting D/H measurements (of column measurements as reported from ground-based observations, and from SO profiles as reported here).

4. Discussion and Conclusions

The challenges faced in the interpretation of D/H and in the context of deriving the history of water on Mars have been nicely summarized in the recent review by Jakosky (2021). Specifically, it is difficult to relate observations of the relatively small atmospheric water column (<100 pr-um GEL) to the current water reservoirs (30–40 m GEL) and to suggested ancient water reservoirs (up to 500 m GEL) with respect to their role in the loss of water to space over Mars’ history. There is also a fractionation effect (of at least 15%) between the D/H in the ice stored in the caps and the D/H observed in the vapor phase (Montmessin et al., 2005). The new results presented here, which probe the vertical profiles of water and D/H for both seasonal caps, together with previous ground-based and orbital measurements, suggest a common and highly enriched value for this labile reservoir of water. Atmospheric D/H behaves as an integrator of the differential individual atomic (H and D) escape rates, and therefore without any new supply of water into the system, the D/H of the labile sources will continue to increase. Among other phenomena, the chaotic changes in obliquity that Mars has experienced (e.g., Laskar et al., 2004), and the corresponding impact on climate and regions of ice stability (e.g., Jakosky et al., 1995; Levrard et al., 2007), could lead to large exchanges between the reservoirs and further homogenization of the D/H across the planet.

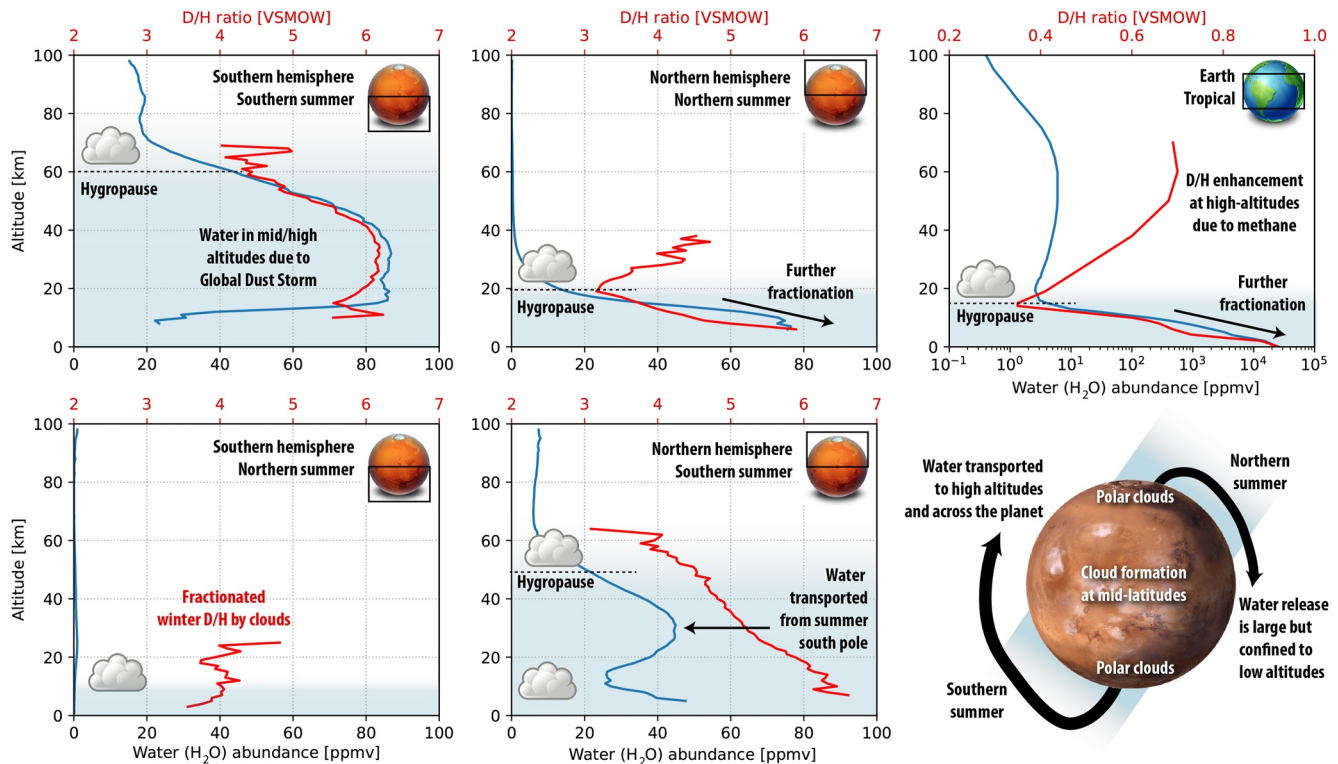


Figure 2. Average water (blue trace) and D/H (red trace) profiles during local summer (upper panels) and local-winter (lower-panels). Southern summer is L_s 240–290 MY34, northern summer is L_s 70–120 MY35. Fractionation across the atmosphere is quite strong as shown in Figure 1, with the D/H being highly affected by the local climate. Therefore, these average profiles are primarily relevant when exploring general vertical morphologies, not for extracting absolute values. During southern summer and the global dust storm (GDS), water is brought to high altitudes, and it is also transported effectively to the winter hemisphere. During northern summer, the hygro-pause is quite compact and the D/H shows a strong fractionation with altitude, similarly to what occurs in our planet (Villanueva et al., 2012).

Thus, the D/H value of the polar caps could be similar to the modern labile D/H value observed in the seasonal releases. This exchange and deposit from the atmosphere to the polar caps could occur rapidly (m/year) or slowly (μ m/year) across millions of years.

Another challenge to the interpretation of D/H is establishing how closed the current hydrological system really is. As water at Mars' ancient value of D/H is added to the system from previously or periodically isolated reservoirs, the D/H ratio of the current hydrological system is lowered. This effect is opposite that of escape to space. One thing is certain, the current D/H is highly enriched, with respect to the H_2 nebular value (0.13 VSMOW, Lellouch et al., 2001), relative to the ancient value of Mars as derived from meteoric records (~ 1.3 VSMOW, 4.5 billion years ago, Usui et al., 2012), and compared to the value of water on Mars during late Hesperian as inferred from rock sampling (~ 3 VSMOW, Mahaffy et al., 2015), or even with respect to primordial cometary value (~ 1 – 3 VSMOW, e.g., Altwegg et al., 2015; Bockelée-Morvan et al., 2015; Villanueva et al., 2009). As water is released by geological activity, with a D/H value resembling the primordial VSMOW value, the effect of this release would be to lower D/H over time. Thus, the integrated water loss implied by the measured D/H is a lower limit. In addition, water and hydrogen-rich volatiles delivered by comets and asteroids would lower the measured D/H value, though current delivery rates suggest a small contribution. Considering the upper bound of the estimates of carbon delivery by comets of $\sim 1E5$ kg/year (Frantseva et al., 2018), and assuming a C/H value of 1 with a constant delivery over 4.5 billion years, one calculates just $4.5E14$ kg (3 mm GEL of water) of water delivered by comets. Such delivery is also comparable to the impact of a 5 km comet, meaning that thousands of comets would need to hit Mars to affect its D/H.

As we explore the history of water on Mars, these new D/H vertical profiles will require additional context provided by other isotopic markers (carbon, oxygen, noble gases), measurements of the formation of ice particles in the atmosphere, and the condensation/accumulation of these particles on the surface. Importantly, the measurements presented here would need to be closely related to subsurface measurements, including potentially groundbreaking measurements obtained by the ESA Rosalind Franklin rover. Furthermore, and hopefully not in

the far future, a measurement of the D/H of the ices in the polar caps could address many of the challenges when interpreting atmospheric D/H values. Measurements obtained below the surface of the polar caps could prove quite revealing in separating current climatological effects and formation processes.

Appendix A: NOMAD Instrument Calibration

The NOMAD instrument onboard TGO has two echelle grating high-resolution spectrometer channels that sample the infrared. One channel is dedicated to SOs and the other to nadir observations (LNO). The measurements presented in this paper pertain to the SO channel, for which we report in this appendix a set of improved calibration methods ensuring an accurate representation of the different subcomponents of the channel. In an echelle spectrometer, the separation is achieved by placing a grating at a specific blaze angle, leading to constructive/destructive patterns at specific resonance orders. These orders will by default overlap spatially on the detector, and typically separation of orders is achieved by placing an order filter switch or a cross-disperser that spatially displaces the orders so they do not overlap. In NOMAD, order sorting is achieved with an AOTF tuned at a specific resonance frequency and with a spectral bandwidth of $\sim 22 \text{ cm}^{-1}$. AOTF filters have a sinc-like response function, and therefore light from nearby orders is also transmitted, although at an attenuated rate. If, hypothetically 5% of nearby orders beyond ± 4 orders are added to the signal, then $5 \times (4 \times 2)$ up to 40% excess flux is added to the measurement, and the main signature is diluted to only $\sim 70\%$ [$100\% / (100\% + 40\%)$], with 30% foreign signature. Capturing these proportions for many different tuning frequencies, and defining exactly how much signal is added from every nearby order is therefore of great importance in assessing the intensity of the observed signals. Our methods to measure and calibrate the AOTF response is described in Section A1.

Another important parameter to be quantified is how the light is dispersed and diffracted by the grating system. This will impact the shape of the observed features (ILS), the intensity of the flux across the order (grating blaze response), and the position of the lines on the detector (spectral calibration). A new characterization of the ILS is presented in Section A2, and a parameterization for the response of the grating with temperature and across orders is presented in Section A3. Detailed calibration scripts using these methods are available at our GitHub (<https://github.com/nasapsg/ExoMars>), documentation at Goddard's ExoMars archive (<https://psg.gsfc.nasa.gov/apps/exomars.php>), and at BIRA's NOMAD site (<https://nomad.aeronomie.be>).

A1. Characterization of the Acousto-Optical-Tunable-Filter

To characterize the response function of the filters across the whole spectral range of the SO channel, we make use of solar “miniscans” and “full-scans.” In this mode, the instrument points to the Sun, and the AOTF scans different frequencies in small increments ($\sim 0.15\text{--}1.2 \text{ cm}^{-1}$); the measurement is repeated several times across a range from 40 to 300 cm^{-1} . The intensity of any solar feature will then change depending on the level of contribution of that order to the whole ensemble, peaking when the AOTF is tuned exactly at the frequency of the solar line. We identified 11 solar lines in the SO range that are relatively well isolated and do not overlap signatures in nearby orders. We then analyzed the whole NOMAD calibration archive (2018–2021) and identified $\sim 70,000$ miniscan spectra that targeted these lines. We then employed two complementary yet independent methods to mine the data and then combined the results from both to establish a calibration scheme for the AOTF.

AOTF shape characterization (“A” method). Starting with our calibration recipe of the AOTF and the grating as reported in Liuzzi et al. (2019), we compute a synthetic a solar spectrum for the center AOTF frequency and the ± 6 orders and perform the order addition with an a priori AOTF solution. We then compare that to the data and determine small frequency shifts (mostly due to thermal–mechanical effects, see Section A3). We then compute two synthetic spectra (a: flux from central order spectrum, and b: flux from all other orders), and determine how much each contributes to the measured spectrum by performing a linear mixing fit. The output of this is a number that indicates how strong the central order is “seen” in the measured spectra. This information is recorded across all miniscans and for the 11 lines (see an example plot for one line in Figure A1). We then take all these measurements for every line, and adopting a specific AOTF model resulting from an initial visual inspection of the results, fit four AOTF parameters: (a) the width of first-crossing of the AOTF (width [cm^{-1}]), (b) the intensity of sidelobes with respect to a perfect sinc, (c) a scaling factor the lower orders with respect to the higher orders (asymmetry factor), and (d) the peak intensity of a broad continuous contribution modeled as a Gaussian with a sigma of 50 cm^{-1} (peak offset). Fits to the miniscans for the 11 solar lines using this method are presented in Figure A1.

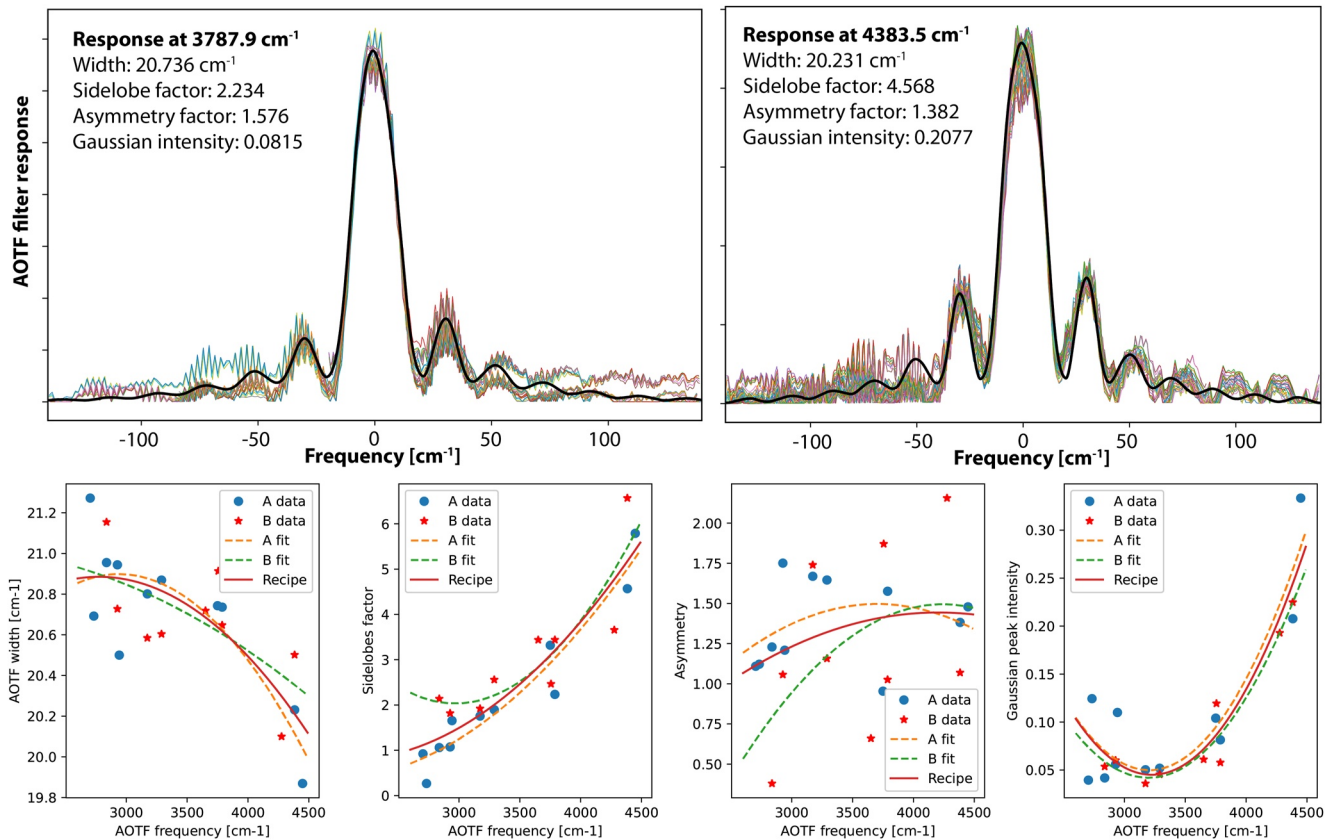


Figure A1. Characterization of Acousto-Optical-Tunable-Filter (AOTF) of the NOMAD solar-occultation (SO) channel. The upper two panels present example miniscan measurements of the intensity of the main order across AOTF frequency for two solar lines, derived employing the “A” method. On these, spectra 4 AOTF parameters were derived, in which this process was repeated for 11 solar lines. The lower panel presents these four parameters as derived employing “A” and “B” methods and the corresponding fits. In our analysis, we employ the solution labeled “recipe” which collects information and results from both methods.

AOTF global fitting (“B” method). The spectra of all miniscans related to a specific line (± 3 cm⁻¹ from a solar line; 1,000–10,000 spectra per line) are combined into a supraspectrum that contains all the measurements. Each measurement is calibrated for baselines and slight frequency corrections by comparing to an a priori solar spectrum. The above mentioned four AOTF parameters are then fitted simultaneously using this supraspectrum as input and employing a Levenberg–Marquardt minimization algorithm. This method, when compared to the “A” method, eliminates one analysis step yet it may be more susceptible to numerical instabilities.

Both techniques provide a metric for the same filter response and therefore are ultimately complementary. As such, we derive the AOTF calibration recipe across tuning frequency (order) by fitting a second-order polynomial to these measurements and by weighting the “A” and “B” results equally. The points do show some scatter, yet the critical parameter width and sidelobe ratio are relatively well constrained. The coefficients for each calibration recipe and the plots presenting the fits are presented in Figure A1

A2. Characterization of the Instrumental Line Shape Function

The ILS describes how the instrument responds to monochromatic light. The observed spectrum is a convolution of the occultation spectrum with the ILS. The main property that describes the ILS is the width, normally quantified as the resolving power $\lambda/\delta\lambda$, which defines the FWHM across wavelength. The resolution of grating

spectrometers is defined by the properties of the grating grooves and the width of the entrance slit. Intrinsically, the ILS of a grating system is a sinc function with a Gaussian core (Villanueva et al., 2013), yet it can be modeled successfully with a Gaussian kernel. When analyzing SO data, we realized that the “left” (lower pixels) side of the spectrum was sharper than the “right” (higher pixels). In some bright lines, a double peak feature could be observed only on the right side of the array and for certain orders (Thomas et al., 2021). This was an unexpected feature of the spectrum, though such effects can occur if a crack develops in a certain element of the optics, leading to a “ghost” image to be produced. In order to characterize this effect, we analyzed Mars occultation data for several orders employing primarily two techniques:

Deconvolution (“C” method). The deconvolution method uses the information content of a spectrum in a completely agnostic way, that is, without making any a priori assumption on the functional form of the ILS. This method compares the observed spectrum with a fiducial model that considers the AOTF properties, by performing a sliding convolution between the two as

$$\text{ILS}(j) \cong \int_{-\infty}^{+\infty} y(x_i + \delta) R(v) d\delta \cong \sum_{i=-M}^{+M} \tilde{y}(x_{i+j}) \cdot R(x_i), \quad (\text{A1})$$

where M represents the number of pixels of the observed spectrum around the j th pixel of the observed spectrum, and \tilde{y} indicates the spectrum previously interpolated to the same sampling as the model radiance R to perform the sum. For our analysis, we considered a sliding convolution with M corresponding to $\pm 15\%$ of the spectrum. As j is varied in Equation A1 across the whole observed spectrum, the ILS is reconstructed for each pixel of the observed spectrum. The output of this process is a two-dimensional array with the ILS at each pixel. If we consider that the ILS is a combination of two Gaussians, then at every pixel we would have to fit $2 \times 3 = 6$ parameters (intensity, width, and center position). Yet, remembering that the intrinsic width of the Gaussian function is defined by the grating (the only diffractive element), and assuming that the second Gaussian is a shifted replica of the main Gaussian, the problem is reduced to three parameters (width of both, relative shift of the ghost, and relative intensity of the ghost). To further constrain the fitting for each order, we assumed that the intensity of the relative ghost is constant across pixels and considered a constant resolving power across pixels. Then, we performed a two-dimensional fit on the observed ILS map by fitting a second displacement function between the two Gaussians (three parameters). This was repeated for many orders across the SO channel and considering different levels of line saturation, see results in Figure A2.

Gaussian fitting (“D” method). An alternative method that we also explored was to analyze Mars spectra containing many isolated bands (e.g., from P and R branch lines of CO_2 and CO) across the detector. A double Gaussian function was fitted to every unsaturated line, and the width, separation, and relative intensity were quantified across the detector. This was repeated across several orders and altitudes on Mars, using more than 100,000 spectra for each order. Similarly, to method C, for each order analyzed, a single RP and intensity were derived for each order analyzed, together with the second-order coefficients of the displacement function.

Each presented method is susceptible to different effects, for instance the accuracy of the “C” method depends on the number and diversity of spectral features across the convolution window, while the “D” method is highly susceptible to baseline issues and contamination of other weak lines. To further test the consistency between methods, two independent teams analyzed the calibration data employing “D” method yet using different baseline and Gaussian fitting methods. For our aggregated calibration method, we combine the relative intensity and width from the three analyses and employ the separation function as determined by the “C” method, see results in Figure A2. We incorporated this complex ILS function into our synthetic models by doing the following: (a) the spectrum is simulated at high resolution and convolved with a single Gaussian kernel having a RP of 17,000, which is the average RP measured across all orders; (b) this convolved model spectrum is interpolated employing the displacement Gaussian function with the coefficients as presented in Figure A2; (c) the total model is computed as a summation of these two components as $S = (S_{1\text{ST}} + 0.27S_{2\text{ND}})/1.27$, in which 0.27 is the average “ghost” intensity factor derived for all orders.

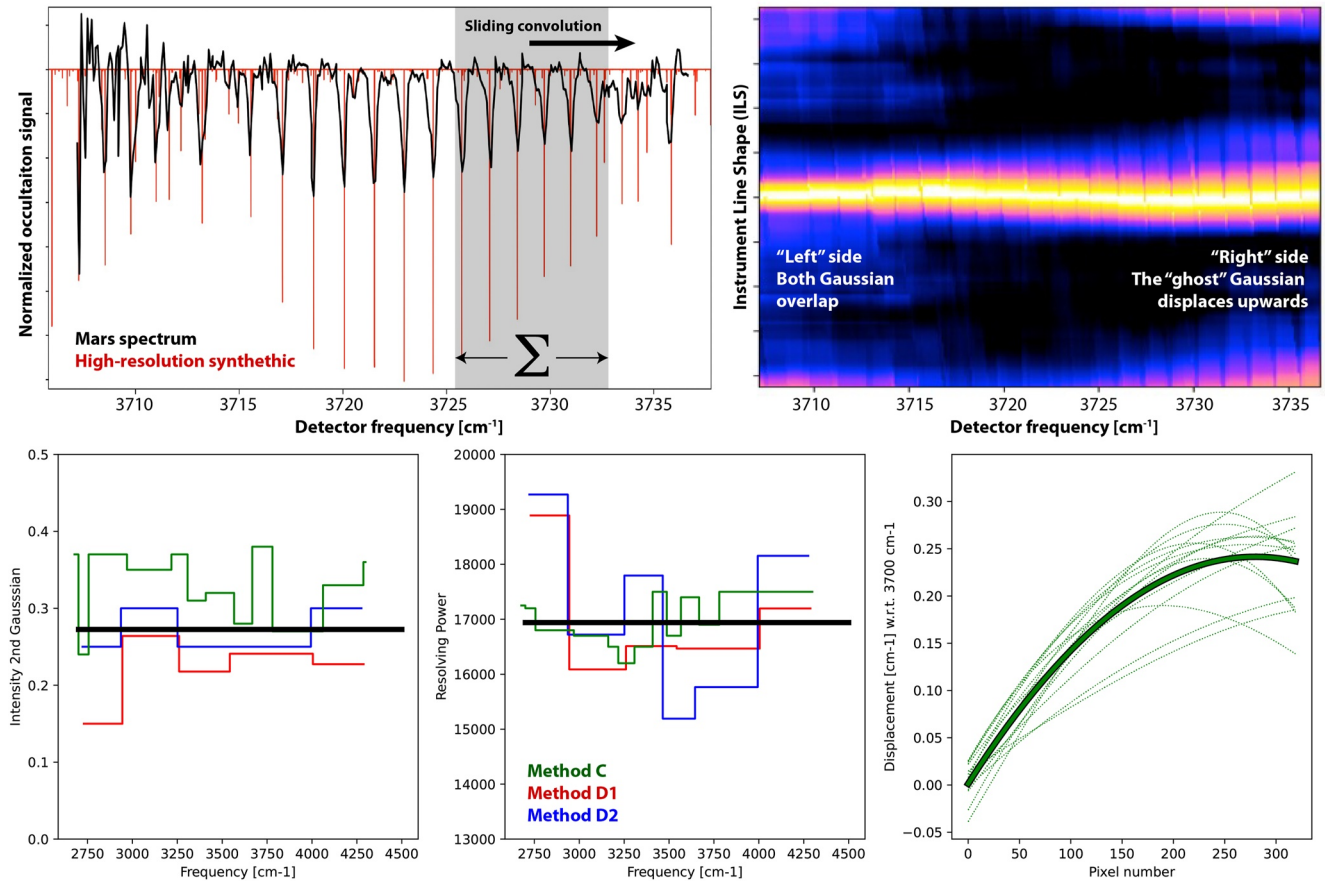


Figure A2. Characterization of Instrument Line Shape (ILS) function of the NOMAD solar-occultation (SO) channel. The upper-left panel shows an example spectrum employed with the “C” method to perform the deconvolution. The red trace is the high-resolution synthetic spectrum, which is convolved with a sliding function across the measured spectrum, resulting in the impulse ILS function. This process is repeated for every pixel in the detector, and an ILS function across the detector is determined (upper-right panel). The lower panel shows the properties of the ILS as determined employing “C” and “D” methods (two independent analyses), while the displacement curve is plotted for all measured orders employing the “C” method in the lower-right panel.

A3. Characterization of the Grating (Width and Position)

The main parameter of the grating is the Free Spectral Range (FSR), which defines the intensity of the blaze across an order and the diffraction projection across pixels (i.e., spectral calibration). In that sense, every detector pixel can be considered a different diffraction system, each having a different FSR, and the anamorphic projection of the dispersive system defining the relationship between pixels and frequency. The relationship between FSR and pixel for the SO channel has been obtained from analyzing full-scan and miniscans as presented in Liuzzi et al. (2019), and $FSR_i = v_i/m = F_0 + F_1 \cdot i + F_2 \cdot i^2$, where i is the pixel number (0–319), v_i is the frequency at pixel i , m is the order, and the coefficients F_0 , F_1 , and F_2 are $2.24734\text{E}+01$, $5.55953\text{E}-04$, and $1.75128\text{E}-08$, respectively. The order number (m) is simply the AOTF frequency (in wavenumbers) divided by the FSR at that pixel.

The peak of the grating transfer function, defined the blaze equation (a sinc squared function), has been tuned in the SO channel to occur near the center pixels (Neefs et al., 2015). The resulting measured flux is then a combination of the flux of all orders filtered through by the AOTF multiplied by the blaze equation. When analyzing calibration data, we noticed that the center of the blaze and therefore “peak” of the grating shifted with frequency for this channel (see upper panel in Figure A3). This would mean that the peak FSR and width of the grating is being affected by refraction or some other optical anomaly, which in turns displaces the peak flux across detector pixels. We used

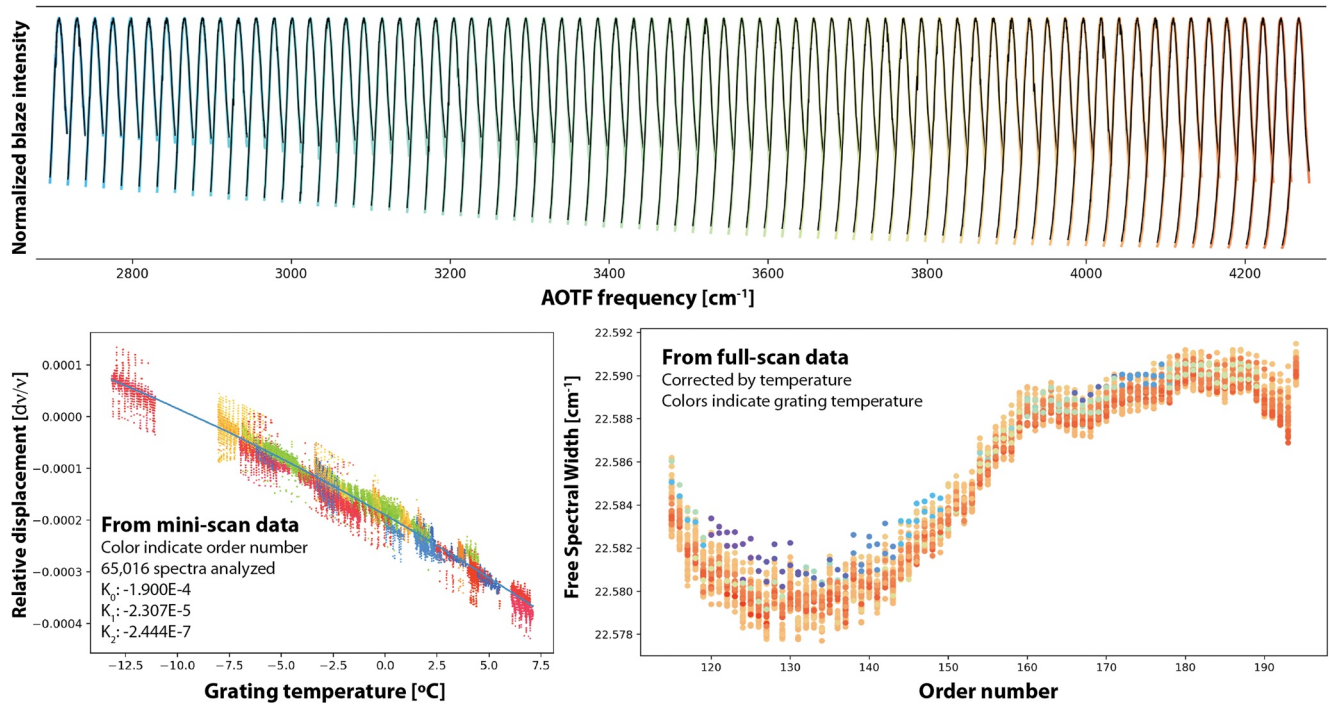


Figure A3. Characterization of grating properties of the NOMAD solar-occultation (SO) channel. The upper panel shows normalized solar spectra collected from full-scan data at different Acousto-Optical-Tunable-Filter (AOTF) frequencies. The overlaid color trace is a synthetic intensity model (PEC function, see Liuzzi et al., 2019) computed using the here presented AOTF and grating calibration solutions, showing very good agreement. The lower-left panel shows the measured spectral displacement of the solar lines sampled in the “A” method for different grating temperatures and order number (color). This dispersion nicely follows a second-order pattern, with coefficients listed in the panel. The frequency of peak Free Spectral Range (FSR; equivalent to the grating width) as shown in the upper panel is plotted in the lower-right panel. These values have been corrected for temperature with all colors generally overlapping, validating the coefficients determined in the lower-left panel. A third-order polynomial was fitted to this curve to identify the variation of the blaze width with order number.

this displacement information to determine the relationship between the grating peak FSR and AOTF frequency as a third degree polynomial: $\text{FSR}_{\text{peak}} = P_0 + P_1 dv + P_2 dv^2 + P_3 dv^3$, where dv is $v_{\text{AOTF}} - 3,700 \text{ cm}^{-1}$, and P_0 , P_1 , P_2 , and P_3 are $2.25863468\text{E}+01$, $9.79270239\text{E}-06$, $-7.20616355\text{E}-09$, and $-1.00162255\text{E}-11$, respectively (see lower-right panel in Figure A3). Since we mostly operate with normalized I/F spectra in our retrievals from SO data, the effect of the FSR_{peak} is not critical for our retrievals, but it is relevant when operating with absolute flux data.

A key aspect of the grating is that its properties are highly susceptible to temperature. As the grating expands and contracts due to variations in temperature, the FSR changes accordingly. We investigated the effects of temperature on the grating by analyzing the variability of FSR_{peak} in the full-scans and that of the shift in the position of lines as determined from the AOTF study (“A” method). In principle, since the spectral solution depends on the grating FSR and grooves spacing, they should expand as $\text{FSR}' = \text{FSR} \cdot [1 + K(T)]$, where $K(T)$ is a scaling correction factor for temperature T (°C). In our analysis of all calibration data from 2018 to 2021 of FSR_{peak} from the full-scans and the line-positions from the miniscans, we observe the same $K(T)$ function, which we determine to be $K(T) = K_0 + K_1 T + K_2 T^2$, where K_0 , K_1 , and K_2 are $-1.90001923\text{E}-04$, $-2.30708836\text{E}-05$, and $-2.44383699\text{E}-07$, respectively (see lower-left panel in Figure A3).

Conflict of Interest

The authors declare no conflicts of interest relevant to this study.

Data Availability Statement

The retrieval software package used in this study is the Planetary Spectrum Generator, free and available online at <https://psg.gsfc.nasa.gov> (Villanueva et al., 2018), with example scripts available at <https://github.com/nasapsg>. The data used in this analysis are available at the European Space Agency (ESA) planetary archive (<https://archives.esac.esa.int/psa>), and also at the NOMAD European data center (<https://nomad.aeronomie.be/index.php/data>, Thomas et al., 2021; Vandaele et al., 2019), and at NASA's ExoMars archive (<https://psg.gsfc.nasa.gov/apps/exomars.php>). Figures were made with Matplotlib version 3.2.1 (Caswell et al., 2020), available under the Matplotlib license at <https://matplotlib.org/>.

Acknowledgments

This work was supported by NASA's Mars Program Office under WBS 604796, "Participation in the TGO/NOMAD Investigation of Trace Gases on Mars." ExoMars is a space mission of the European Space Agency (ESA) and Roscosmos. The NOMAD experiment is led by the Royal Belgian Institute for Space Aeronomy (IASB-BIRA), assisted by Co-PI teams from Spain (IAA-CSIC), Italy (INAF-IAPS), and the United Kingdom (The Open University). This project acknowledges funding by the Belgian Science Policy Office (BELSPO), with the financial and contractual coordination by the ESA Prodex Office (PEA 4000103401, 4000121493), by the Spanish MICINN through its Plan Nacional and by European funds under grants PGC2018-101836-B-I00 and ESP2017-87143-R (MINECO/FEDER) and by the Spanish Science Ministry Centro de Excelencia Severo Ochoa Program under grant SEV-2017-0709, as well as by the UK Space Agency through grants ST/V002295/1, ST/V005332/1, and ST/S00145X/1 and Italian Space Agency through grant 2018-2-HH.0. This work was supported by the Belgian Fonds de la Recherche Scientifique – FNRS (grant number 30442502, ET_HOME) and has received funding from the European Union's Horizon 2020 research and innovation program (grant agreement no. 101004052, RoadMap project). SR thanks BELSPO for the FED-tWIN funding (Prf-2019-077 - RT-MOLEXO).

References

- Alday, J., Trokhimovskiy, A., Irwin, P. G. J., Wilson, C. F., Montmessin, F., Lefèvre, F., et al. (2021). Isotopic fractionation of water and its photolytic products in the atmosphere of Mars. *Nature Astronomy*, 5, 943–950. <https://doi.org/10.1038/s41550-021-01389-x>
- Alday, J., Wilson, C. F., Irwin, P. G. J., Trokhimovskiy, A., Montmessin, F., Fedorova, A. A., et al. (2021). Isotopic composition of CO₂ in the atmosphere of Mars: Fractionation by diffusive separation observed by the ExoMars trace gas orbiter. *Journal of Geophysical Research: Planets*, 126, e2021JE006992. <https://doi.org/10.1029/2021JE006992>
- Altwegg, K., Balsiger, H., Bar-Nun, A., Berthelier, J. J., Bieler, A., Bochsler, P., et al. (2015). 67P/Churyumov-Gerasimenko, a Jupiter family comet with a high D/H ratio. *Science*, 347, 1261952. <https://doi.org/10.1126/science.1261952>
- Aoki, S., Vandaele, A. C., Daerden, F., Villanueva, G. L., Liuzzi, G., Thomas, I. R., et al. (2019). Water vapor vertical profiles on Mars in dust storms observed by TGO/NOMAD. *Journal of Geophysical Research: Planets*, 124, 3482–3497. <https://doi.org/10.1029/2019JE006109>
- Belyaev, D. A., Fedorova, A. A., Trokhimovskiy, A., Alday, J., Montmessin, F., Korabiev, O. I., et al. (2021). Revealing a high water abundance in the upper mesosphere of Mars with ACS onboard TGO. *Geophysical Research Letters*, 48, e2021GL093411. <https://doi.org/10.1029/2021GL093411>
- Bibring, J.-P., Langevin, Y., Mustard, J. F., Poulet, F., Arvidson, R., Gendrin, A., et al. (2006). Global mineralogical and aqueous Mars history derived from OMEGA/Mars express data. *Science*, 312, 400–404. <https://doi.org/10.1126/science.1122659>
- Bockelée-Morvan, D., Calmonte, U., Charnley, S., Duprat, J., Engstrand, C., Gicquel, A., et al. (2015). Cometary isotopic measurements. *Space Science Reviews*, 197, 1–83. <https://doi.org/10.1007/s11214-015-0156-9>
- Brain, D. A., McFadden, J. P., Halekas, J. S., Connerney, J. E. P., Bougher, S. W., Curry, S., et al. (2015). The spatial distribution of planetary ion fluxes near Mars observed by MAVEN. *Geophysical Research Letters*, 42, 9142–9148. <https://doi.org/10.1002/2015GL065293>
- Byrne, S., & Murray, B. C. (2002). North polar stratigraphy and the Paleo-erg of Mars. *Journal of Geophysical Research*, 107(E6), 5044. <https://doi.org/10.1029/2001JE001615>
- Carr, M. H., & Head, J. W. (2003). Oceans on Mars: An assessment of the observational evidence and possible fate. *Journal of Geophysical Research*, 108(E5), 5042. <https://doi.org/10.1029/2002JE001963>
- Caswell, T. A., Droettboom, M., Lee, A., Hunter, J., Firing, E., Stansby, D., et al. (2020). Matplotlib/matplotlib v3.1.3. *Zenodo*. <https://doi.org/10.5281/zenodo.3633844>
- Chaffin, M. S., Kass, D. M., Aoki, S., Fedorova, A. A., Deighan, J., Connour, K., et al. (2021). Martian water loss to space enhanced by regional dust storms. *Nature Astronomy*, 5, 1036–1042. <https://doi.org/10.1038/s41550-021-01425-w>
- Crismani, M. M. J., Villanueva, G. L., Liuzzi, G., Smith, M. D., Knutsen, E. W., Daerden, F., et al. (2021). A global and seasonal perspective of Martian water vapor from ExoMars/NOMAD. *Journal of Geophysical Research: Planets*, 126, e2021JE006878. <https://doi.org/10.1029/2021JE006878>
- Daerden, F., Neary, L., Villanueva, G., Liuzzi, G., Aoki, S., Clancy, R. T., et al. (2022). Explaining NOMAD D/H observations by cloud-induced fractionation of water vapor on Mars. *Journal of Geophysical Research: Planets*, 127, e2021JE007079. <https://doi.org/10.1029/2021JE007079>
- Daerden, F., Whiteway, J. A., Davy, R., Verhoeven, C., Komguem, L., Dickinson, C., et al. (2010). Simulating observed boundary layer clouds on Mars. *Geophysical Research Letters*, 37, L04203. <https://doi.org/10.1029/2009GL041523>
- Devi, V. M., Benner, D. C., Sung, K., Crawford, T. J., Gamache, R. R., Renaud, C. L., et al. (2017). Line parameters for CO₂- and self-broadening in the ν_3 band of HD¹⁶O. *Journal of Quantitative Spectroscopy and Radiative Transfer*, 203, 158–174. <https://doi.org/10.1016/j.jqsrt.2017.02.020>
- Fedorova, A. A., Montmessin, F., Korabiev, O., Luginin, M., Trokhimovskiy, A., Belyaev, D. A., et al. (2020). Stormy water on Mars: The distribution and saturation of atmospheric water during the dusty season. *Science*, 367, 297–300. <https://doi.org/10.1126/science.aay9522>
- Fishbaugh, K. E., & Head, J. W. (2005). Origin and characteristics of the Mars north polar basal unit and implications for polar geologic history. *Icarus, Mars Polar Science III*, 174, 444–474. <https://doi.org/10.1016/j.icarus.2004.06.021>
- Frantseva, K., Mueller, M., ten Kate, I. L., van der Tak, F. F. S., & Greenstreet, S. (2018). Delivery of organics to Mars through asteroid and comet impacts. *Icarus*, 309, 125–133. <https://doi.org/10.1016/j.icarus.2018.03.006>
- Gordon, I. E., Rothman, L. S., Hargreaves, R. J., Hashemi, R., Karlovets, E. V., Skinner, F. M., et al. (2022). The HITRAN2020 molecular spectroscopic database. *Journal of Quantitative Spectroscopy and Radiative Transfer*, 277, 107949. <https://doi.org/10.1016/j.jqsrt.2021.107949>
- Heavens, N. G., Kleinböhl, A., Chaffin, M. S., Halekas, J. S., Kass, D. M., Hayne, P. O., et al. (2018). Hydrogen escape from Mars enhanced by deep convection in dust storms. *Nature Astronomy*, 2, 126–132. <https://doi.org/10.1038/s41550-017-0353-4>
- Holmes, J. A., Lewis, S. R., Patel, M. R., Chaffin, M. S., Cangi, E. M., Deighan, J., et al. (2021). Enhanced water loss from the Martian atmosphere during a regional-scale dust storm and implications for long-term water loss. *Earth and Planetary Science Letters*, 571, 117109. <https://doi.org/10.1016/j.epsl.2021.117109>
- Houben, H., Haberle, R. M., Young, R. E., & Zent, A. P. (1997). Modeling the Martian seasonal water cycle. *Journal of Geophysical Research*, 102, 9069–9083. <https://doi.org/10.1029/97JE00046>
- Jakosky, B. M. (2021). Atmospheric loss to space and the history of water on Mars. *Annual Review of Earth and Planetary Sciences*, 49, 71–93. <https://doi.org/10.1146/annurev-earth-062420-052845>
- Jakosky, B. M., Henderson, B. G., & Mellon, M. T. (1995). Chaotic obliquity and the nature of the Martian climate. *Journal of Geophysical Research*, 100, 1579–1584. <https://doi.org/10.1029/94JE02801>

- Jakosky, B. M., Slipski, M., Benna, M., Mahaffy, P., Elrod, M., Yelle, R., et al. (2017). Mars' atmospheric history derived from upper-atmosphere measurements of $^{38}\text{Ar}/^{36}\text{Ar}$. *Science*, 355, 1408–1410. <https://doi.org/10.1126/science.aai7721>
- Krasnopolsky, V. A. (2015). Variations of the $\text{HDO}/\text{H}_2\text{O}$ ratio in the Martian atmosphere and loss of water from Mars. *Icarus*, 257, 377–386. <https://doi.org/10.1016/j.icarus.2015.05.021>
- Laskar, J., Correia, A. C. M., Gastineau, M., Joutel, F., Levrard, B., & Robutel, P. (2004). Long term evolution and chaotic diffusion of the insolation quantities of Mars. *Icarus*, 170, 343–364. <https://doi.org/10.1016/j.icarus.2004.04.005>
- Lasue, J., Mangold, N., Hauber, E., Clifford, S., Feldman, W., Gasnault, O., et al. (2013). Quantitative assessments of the Martian hydrosphere. *Space Science Reviews*, 174, 155–212. <https://doi.org/10.1007/s11214-012-9946-5>
- Lellouch, E., Bézard, B., Fouchet, T., Feuchtgruber, H., Encrenaz, T., & de Graauw, T. (2001). The deuterium abundance in Jupiter and Saturn from ISO-SWS observations. *Astronomy and Astrophysics*, 370, 610–622. <https://doi.org/10.1051/0004-6361:20010259>
- Levrard, B., Forget, F., Montmessin, F., & Laskar, J. (2007). Recent formation and evolution of northern Martian polar layered deposits as inferred from a Global Climate Model. *Journal of Geophysical Research*, 112, E06012. <https://doi.org/10.1029/2006JE002772>
- Liuzzi, G., Villanueva, G. L., Mumma, M. J., Smith, M. D., Daerden, F., Ristic, B., et al. (2019). Methane on Mars: New insights into the sensitivity of CH_4 with the NOMAD/ExoMars spectrometer through its first in-flight calibration. *Icarus*, 321, 671–690. <https://doi.org/10.1016/j.icarus.2018.09.021>
- Mahaffy, P. R., Webster, C. R., Stern, J. C., Brunner, A. E., Atreya, S. K., Conrad, P. G., & The MSL Science Team. (2015). The imprint of atmospheric evolution in the D/H of Hesperian clay minerals on Mars. *Science*, 347, 412–414. <https://doi.org/10.1126/science.1260291>
- Montabone, L., Spiga, A., Kass, D. M., Kleinböhl, A., Forget, F., & Millour, E. (2020). Martian year 34 column dust climatology from Mars climate sounder observations: Reconstructed maps and model simulations. *Journal of Geophysical Research: Planets*, 125, e2019JE006111. <https://doi.org/10.1029/2019JE006111>
- Montmessin, F., Fouchet, T., & Forget, F. (2005). Modeling the annual cycle of HDO in the Martian atmosphere. *Journal of Geophysical*, 110, E03006. <https://doi.org/10.1029/2004JE002357>
- Neary, L., & Daerden, F. (2018). The GEM-Mars General Circulation Model for Mars: Description and evaluation. *Icarus*, 300, 458–476. <https://doi.org/10.1016/j.icarus.2017.09.028>
- Neary, L., Daerden, F., Aoki, S., Whiteway, J., Clancy, R. T., Smith, M., et al. (2020). Explanation for the increase in high-altitude water on Mars observed by NOMAD during the 2018 global dust storm. *Geophysical Research Letters*, 47, e2019GL084354. <https://doi.org/10.1029/2019GL084354>
- Neefs, E., Vandaele, A. C., Drummond, R., Thomas, I. R., Berkenbosch, S., Clairquin, R., et al. (2015). NOMAD spectrometer on the ExoMars trace gas orbiter mission: Part 1—Design, manufacturing and testing of the infrared channels. *Applied Optics*, 54, 8494–8520. <https://doi.org/10.1364/AO.54.008494>
- Plaut, J. J., Picardi, G., Safaeinili, A., Ivanov, A. B., Milkovich, S. M., Cicchetti, A., et al. (2007). Subsurface radar sounding of the south polar layered deposits of Mars. *Science*, 316, 92–95. <https://doi.org/10.1126/science.1139672>
- Régalia, L., Cousin, E., Gamache, R. R., Vispoel, B., Robert, S., & Thomas, X. (2019). Laboratory measurements and calculations of line shape parameters of the $\text{H}_2\text{O}-\text{CO}_2$ collision system. *Journal of Quantitative Spectroscopy and Radiative Transfer*, 231, 126–135. <https://doi.org/10.1016/j.jqsrt.2019.04.012>
- Richardson, M. I., & Wilson, R. J. (2002). Investigation of the nature and stability of the Martian seasonal water cycle with a general circulation model. *Journal of Geophysical Research*, 107(E5), 5031. <https://doi.org/10.1029/2001JE001536>
- Rossi, L., Vals, M., Montmessin, F., Forget, F., Millour, E., Fedorova, A., et al. (2021). The effect of the Martian 2018 global dust storm on HDO as predicted by a Mars global climate model. *Geophysical Research Letters*, 48, e2020GL090962. <https://doi.org/10.1029/2020GL090962>
- Scheller, E. L., Ehlmann, B. L., Hu, R., Adams, D. J., & Yung, Y. L. (2021). Long-term drying of Mars by sequestration of ocean-scale volumes of water in the crust. *Science*, 372, 56–62. <https://doi.org/10.1126/science.abc7717>
- Stone, S. W., Yelle, R. V., Benna, M., Lo, D. Y., Elrod, M. K., & Mahaffy, P. R. (2020). Hydrogen escape from Mars is driven by seasonal and dust storm transport of water. *Science*, 370, 824–831. <https://doi.org/10.1126/science.aba5229>
- Thomas, I. R., Aoki, S., Trompet, L., Robert, S., Depiesse, C., Willame, Y., et al. (2021). Calibration of NOMAD on ESA's ExoMars trace gas orbiter: Part 1—The solar occultation channel. *Planetary and Space Science*, 105411. <https://doi.org/10.1016/j.pss.2021.105411>
- Usui, T., Alexander, C. M. O., Wang, J., Simon, J. I., & Jones, J. H. (2012). Origin of water and mantle–crust interactions on Mars inferred from hydrogen isotopes and volatile element abundances of olivine-hosted melt inclusions of primitive shergottites. *Earth and Planetary Science Letters*, 357, 119–129. <https://doi.org/10.1016/j.epsl.2012.09.008>
- Vandaele, A. C., Korabiev, O., Daerden, F., Aoki, S., Thomas, I. R., Altieri, F., et al. (2019). Martian dust storm impact on atmospheric H_2O and D/H observed by ExoMars trace gas orbiter. *Nature*, 568, 521–525. <https://doi.org/10.1038/s41586-019-1097-3>
- Villanueva, G. L., Liuzzi, G., Crismani, M. M. J., Aoki, S., Vandaele, A. C., Daerden, F., et al. (2021). Water heavily fractionated as it ascends on Mars as revealed by ExoMars/NOMAD. *Science Advances*, 7, eabc8843. <https://doi.org/10.1126/sciadv.abc8843>
- Villanueva, G. L., Mumma, M. J., Bonev, B. P., Di Santi, M. A., Gibb, E. L., Bönnhardt, H., & Lippi, M. (2009). A sensitive search for deuterated water in comet 8P/Tuttle. *The Astrophysical Journal Letters*, 690, L5–L9. <https://doi.org/10.1088/0004-637X/690/1/L5>
- Villanueva, G. L., Mumma, M. J., Bonev, B. P., Novak, R. E., Barber, R. J., & Disanti, M. A. (2012). Water in planetary and cometary atmospheres: $\text{H}_2\text{O}/\text{HDO}$ transmittance and fluorescence models. *Journal of Quantitative Spectroscopy and Radiative Transfer*, 113, 202–220. <https://doi.org/10.1016/j.jqsrt.2011.11.001>
- Villanueva, G. L., Mumma, M. J., Novak, R. E., Käufel, H. U., Hartogh, P., Encrenaz, T., et al. (2015). Strong water isotopic anomalies in the Martian atmosphere: Probing current and ancient reservoirs. *Science*, 348, 218–221. <https://doi.org/10.1126/science.aaa3630>
- Villanueva, G. L., Mumma, M. J., Novak, R. E., Radeva, Y. L., Käufel, H. U., Smette, A., et al. (2013). A sensitive search for organics (CH_4 , CH_3OH , H_2CO , C_2H_6 , C_2H_2 , C_2H_4), hydroperoxyl (HO_2), nitrogen compounds (N_2O , NH_3 , HCN) and chlorine species (HCl , CH_3Cl) on Mars using ground-based high-resolution infrared spectroscopy. *Icarus*, 223, 11–27. <https://doi.org/10.1016/j.icarus.2012.11.013>
- Villanueva, G. L., Smith, M. D., Protospapa, S., Faggi, S., & Mandell, A. M. (2018). Planetary Spectrum Generator: An accurate online radiative transfer suite for atmospheres, comets, small bodies and exoplanets. *Journal of Quantitative Spectroscopy and Radiative Transfer*, 217, 86–104. <https://doi.org/10.1016/j.jqsrt.2018.05.023>
- Whiteway, J. A., Komguem, L., Dickinson, C., Cook, C., Illnicki, M., Seabrook, J., et al. (2009). Mars water-ice clouds and precipitation. *Science*, 325, 68–70. <https://doi.org/10.1126/science.1172344>
- Zuber, M. T., Smith, D. E., Solomon, S. C., Abshire, J. B., Afzal, R. S., Aharonson, O., et al. (1998). Observations of the north polar region of Mars from the Mars orbiter laser altimeter. *Science*, 282, 2053–2060. <https://doi.org/10.1126/science.282.5396.2053>